Journal of Computational Physics **170,** 614–641 (2001)
doi:10.1006/jcph.2001.6753, available online at http://www.idealibrary.com on IDEAL®

Phase-Accuracy Comparisons and Improved Far-Field Estimates for 3-D Edge Elements on Tetrahedral Meshes

Peter Monk*,[1] and Kevin Parrott†,[2]

*Department of Mathematical Sciences, University of Delaware, Newark, Delaware 19711;
†Computing and Mathematical Sciences, University of Greenwich,
30 Park Row, London, SE10 9LS, United Kingdom
E-mail: monk@math.udel.edu; a.k.parrott@gre.ac.uk

Received April 12, 2000; revised December 20, 2000

Edge-element methods have proved very effective for 3-D electromagnetic computations and are widely used on unstructured meshes. However, the accuracy of standard edge elements can be criticised because of their low order. This paper analyses discrete dispersion relations together with numerical propagation accuracy to determine the effect of tetrahedral shape on the phase accuracy of standard 3-D edge-element approximations in comparison to other methods. Scattering computations for the sphere obtained with edge elements are compared with results obtained with vertex elements, and a new formulation of the far-field integral approximations for use with edge elements is shown to give improved cross sections over conventional formulations.

Key Words: Maxwell's equations; edge elements; dispersion relations; tetrahedral meshes.

1. INTRODUCTION

Accurate electromagnetic wave propagation computations are required in areas such as radar cross-section calculations, antenna design, electromagnetic compatibility modelling, and microwave tomography. Edge-element methods are one of the methods in active use in all these applications; however, despite their popularity, the inherent accuracy of the standard edge element is not easily analysed, lying somewhere between first and second order. Higher order edge elements provide better convergence rates [12] but are relatively expensive when used on unstructured meshes. Conforming elements encounter severe difficulties with

[1] Research supported in part by AFOSR.
[2] Research supported in part by EPSRC/DTI and BAe.

0021-9991/01 $35.00

singularities at rentrant corners in 3D and are currently not an option for such domains, although recent work [1, 2] on singularity subtraction has shown some success in 2D.

Maxwell's equations in free space are a first-order hyperbolic system, but can be reformulated in a wide variety of ways, e.g., as second-order vector wave equations in either of the two electromagnetic fields, or as complex vector Helmholtz problems in the frequency domain. This paper uses time-domain implementations for the numerical testing (allowing efficient broadband comparisons to be made); however, the results are also relevant to the frequency domain. We analyse edge-element approximation of the first-order system, partly for ease of comparison with finite-difference time-domain (FDTD) and the conforming element method. However, it should be noted that this formulation is equivalent to an edge-element approximation of the second-order electric field wave equation.

The edge-element method has been proposed by numerous authors. The interpolation properties of these elements were analysed by Nédélec [38]. Their use in low-frequency eddy current problems is reviewed in [9], and for time-harmonic scattering see [14]. We restrict our study to the lowest order elements which are related to Whitney forms [8] and have been discovered independently by Cendes and co-workers [6]. The use of these elements in the time domain has been examined by Lee and co-workers (see [19, 20], and references therein). The same elements have also been investigated in the context of radar calculations in [23, 24] where suitable absorbing boundary conditions are discussed in some detail (see also [11]). For a full history of the elements, as well as many useful practical details, see Jin [17]. We have not considered related approaches, such as the the co-volume approach of [16, 25] since they are restricted to Delaunay–Voronoi meshes.

In this paper we are specifically concerned with the accuracy of the edge-element method for electromagnetic wave propagation, when used on unstructured meshes. We also describe how to obtain improved estimates of far-field quantities when the method is used for scattering calculations. Reference points for this assessment are provided by the Yee finite-difference scheme and conforming linear elements [33], and the main tools used are discrete dispersion relations and numerical comparisons of results for wave propagation. Scattering from a sphere was used to provide more realistic, albeit qualitative, tests of wave propagation for edge elements and for conforming linear elements (see also [31]).

The scattering coefficent depends on far-field quantities which are themselves surface integrals of computed near fields; the low-order nature of edge elements makes these integrals awkward to approximate. Conventional finite-element approximations of fluid flow or heat transfer have a similar difficulty in retaining their accuracy when approximating flux integrals. The approach taken [3–5, 46] is to reformulate the integral in a variational form; we show that this approach can be applied in 3D to the far-field integrals (see [32] for a 2-D formulation), resulting in a novel formulation which significantly improves the accuracy of broadband scattering computations using edge elements.

1.1. *Finite-Element Approximation of Maxwell's Equations*

Maxwell's equations for the electric field $\mathbf{E}$ and the magnetic field $\mathbf{H}$ on an isotropic nonconducting domain Ω are

$$\epsilon \mathbf{E}_t - \nabla \times \mathbf{H} = 0, \tag{1.1a}$$

$$\mu \mathbf{H}_t + \nabla \times \mathbf{E} = 0. \tag{1.1b}$$

These equations can be written in a weak form, for any sufficiently smooth functions $\phi(x, y, z), \psi(x, y, z) \in (L^2(\Omega))^3$, as

$$\left(\epsilon \frac{\partial \mathbf{E}}{\partial t}, \psi\right) - (\nabla \times \mathbf{H}, \psi) = 0, \tag{1.2a}$$

$$\left(\mu \frac{\partial \mathbf{H}}{\partial t}, \phi\right) + (\nabla \times \mathbf{E}, \phi) = 0, \tag{1.2b}$$

where $(\psi, \phi) = \int_\Omega \psi \cdot \phi \, dV$.

A finite-element approximation to the electromagnetic fields can be written in the form

$$\mathbf{E}_h(\mathbf{x}, t) = \sum_{i=1}^{N_E} E_i(t) \psi_{h,i}(\mathbf{x}) \quad \text{and} \quad \mathbf{H}_h(\mathbf{x}, t) = \sum_{j=1}^{N_H} H_j(t) \phi_{h,j}(\mathbf{x}) \quad \forall \mathbf{x} \in \Omega^h, \tag{1.3}$$

where $E_i(t)$ and $H_j(t)$ are time-dependent degrees of freedom, N_E and N_H are the number of degrees of freedom for each field, and $\psi_{h,i}$ and $\phi_{h,j}$ are finite element basis functions. In the formulations described below, the domain of interest Ω has been covered by an unstructured tetrahedral mesh Ω_h consisting of N_t tetrahedra of maximum diameter h, with N_e edges, N_f faces, and N_v vertices.

1.1.1. Edge elements. This paper is principally concerned with the first-order Nedelec elements where, in (1.3), E_i are the tangential electric field components on each edge, and H_j are face normal components of the magnetic flux. The numbers of degrees of freedom for the two fields are then $N_E = N_e$ and $N_B = N_f$. The electric field basis function for the ith edge, of length s_i and connecting vertices $\{m, n\}$, is given by

$$\psi_{h,i}(\mathbf{x}) = s_i(\varphi_m \nabla \varphi_n - \varphi_n \nabla \varphi_m), \tag{1.4}$$

where φ is the conventional piecewise-linear basis function, taking a value 1 at vertex m and 0 at any other vertex. It is sometimes convenient to combine the edge length with the degrees of freedom.

The magnetic flux basis function for the jth face, connecting vertices $\{l, m, n\}$, and of area A_j is

$$\phi_{h,j}(\mathbf{x}) = 2A_j[\varphi_l(\nabla \varphi_m \times \nabla \varphi_n) + \varphi_m(\nabla \varphi_n \times \nabla \varphi_l) + \varphi_n(\nabla \varphi_l \times \nabla \varphi_m)]. \tag{1.5}$$

The numbers of degrees of freedom for these elements are consequently $N_E = N_e$ and $N_B = N_f$. Since they do not have a well-defined curl, (1.2a) is first integrated by parts so that the semidiscrete edge-element approximations to (1.2) are

$$\left(\epsilon \frac{\partial \mathbf{E}_h}{\partial t}, \psi_h\right) - (\mathbf{H}_h, \nabla \times \psi_h) = -\langle \mathbf{H}_h \times \nu, \psi_h \rangle, \tag{1.6a}$$

$$\left(\mu \frac{\partial \mathbf{H}_h}{\partial t}, \phi_h\right) + (\nabla \times \mathbf{E}_h, \phi_h) = 0, \tag{1.6b}$$

where $\langle \phi, \psi \rangle = \int_{\partial \Omega^h} \phi \cdot \psi \, dS$ and ν is the outward facing normal on $\partial \Omega_h$. The boundary term in (1.6a) either will be zero or will be used to weakly impose an absorbing boundary condition (see Section 4). The electric-field approximation is that of the standard first-order

edge-element method. It can be seen from (1.4), (1.5), and (1.6b) that the time derivative (time difference in the fully discrete case) of the magnetic field degrees of freedom is exactly the discrete curl of the electric field. It is straightforward to show that this formulation is equivalent to an edge-element method used directly on the second-order electric-field problem.

1.1.2. Vertex elements. In the case of linear vertex elements the electric and magnetic fields are treated identically, and the degrees of freedom for each field are the Cartesian components at each vertex of the mesh. The basis functions for each field are identical; there is one for each field component at a given vertex so that those at the kth vertex can be denoted by

$$\psi_{h,3k+\alpha} = \phi_{h,3k+\alpha} = \varphi_k(\mathbf{x})\mathbf{e}_\alpha, \quad \alpha = 0, 1, 2, \tag{1.7}$$

where $\mathbf{e}_\alpha$ are the Cartesian unit vectors. Clearly in this case $N_E = N_B = 3N_v$. The semi-discrete vertex-element equations are then

$$\left(\epsilon \frac{\partial \mathbf{E}_h}{\partial t}, \phi_h\right) - (\nabla \times \mathbf{H}_h, \phi_h) = 0, \tag{1.8a}$$

$$\left(\mu \frac{\partial \mathbf{H}_h}{\partial t}, \phi_h\right) + (\nabla \times \mathbf{E}_h, \phi_h) = 0, \tag{1.8b}$$

and are well defined for these elements, although integration by parts can be used to allow weak imposition of boundary conditions (see Section 4).

We note here that vertex elements require storage of fewer degrees of freedom on a tetrahedral mesh. However, they are currently limited to problems with no singularities (e.g., from re-entrant corners), and although they can be applied to heterogeneous problems they are not as well suited to these as are edge elements. On the other hand edge elements give a partially discontinuous representation even when the solution is known to be smooth (e.g., for wave propagation in free space).

2. DISPERSION RELATIONS ON TETRAHEDRAL MESHES

2.1. *Regular Tetrahedral Meshes*

An important method of characterising the properties of any numerical approximation to the wave equation is to derive its discrete dispersion properties through a Fourier analysis. In this section we do this for semi-discrete schemes (1.6) and (1.8) on regular tetrahedral meshes and make comparisons (where possible) with the Yee finite-difference scheme as a benchmark.

A translation-invariant grid of $\mathbf{R}^3$ is required for the analysis; consider a reference "unit cell" $\hat{\Omega}$ of unit volume. This unit cell is a polyhedron meshed by tetrahedra, and we suppose that there are three independent vectors $\mathbf{v}_1$, $\mathbf{v}_2$, and $\mathbf{v}_3$ such that if $\hat{\Omega}$ is translated by integer multiples of the three vectors, then we generate a finite-element mesh of $\mathbf{R}^3$. This mesh is then scaled by an overall scale factor h (this is equivalent to meshing $\mathbf{R}^3$ using translates of the scaled unit cell $\Omega_h = h\hat{\Omega}$).

The continuous problem (1.1) has a plane-wave solution proportional to $\exp(i(\mathbf{k}\cdot\mathbf{x} - \omega t))$, where for convenience we have set light speed $1/(\mu\epsilon)^{1/2}$ to unity, provided either of

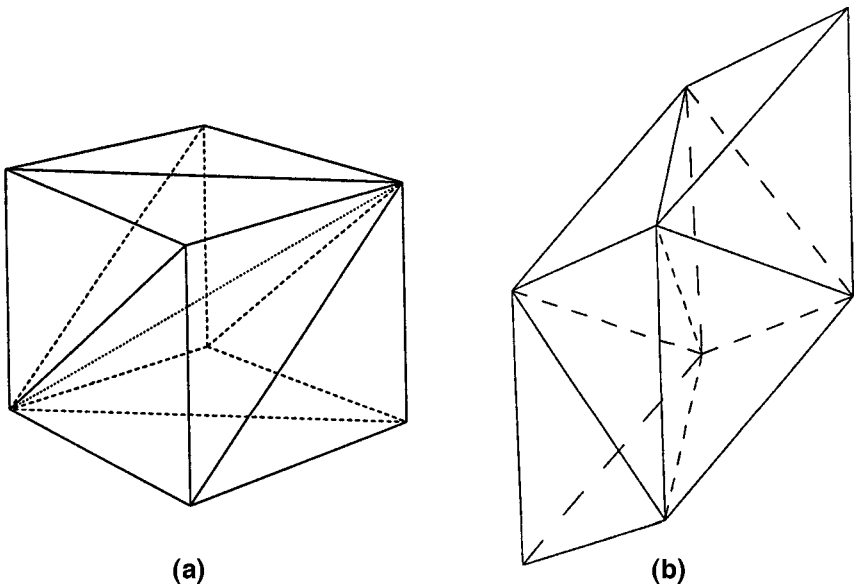

FIG. 1. Two types of unit cells used in the dispersion analysis. (a) Cubic unit cell subdivided into six tetrahedra; (b) Sommerville unit cell divided into six congruent tetrahedra.

the dispersion relations $\omega = 0$ or $\omega = \pm|\mathbf{k}|$ is satisfied. Discrete plane-wave solutions of (1.6) and (1.8) are then sought, of the form

$$\mathbf{E}_h(\mathbf{x}, t) = \hat{\mathbf{E}}_h(\mathbf{x})\exp(-i\omega_h t) \quad \text{and} \quad \mathbf{H}_h(\mathbf{x}, t) = \hat{\mathbf{H}}_h(\mathbf{x})\exp(-i\omega_h t),$$

where $\hat{\mathbf{E}}_h$ and $\hat{\mathbf{H}}_h$ have the translation property that for every $\mathbf{x} \in \mathbf{R}^3$

$$\hat{\mathbf{E}}_h(\mathbf{x} + lh\mathbf{v}_1 + mh\mathbf{v}_2 + nh\mathbf{v}_3) = \hat{\mathbf{E}}_h(\mathbf{x})\exp(i\mathbf{k}\cdot(lh\mathbf{v}_1 + mh\mathbf{v}_2 + nh\mathbf{v}_3))$$
$$\hat{\mathbf{H}}_h(\mathbf{x} + lh\mathbf{v}_1 + mh\mathbf{v}_2 + nh\mathbf{v}_3) = \hat{\mathbf{H}}_h(\mathbf{x})\exp(i\mathbf{k}\cdot(lh\mathbf{v}_1 + mh\mathbf{v}_2 + nh\mathbf{v}_3))$$

for integers *l*, *m*, and *n*. For these functions to satisfy the finite-element equations, the vector $\mathbf{k}$ and the frequency ω_h have to be related by a dispersion relation $\omega_h = \omega_h(\mathbf{k}, h)$. Since the shape of the tetrahedra influences the accuracy of this relation, we shall consider two different meshes, one based on right tetrahedra and another based on Sommerville tetrahedra, as shown in Fig. 1. The unit cell in the Sommerville case is a polyhedron consisting of six Sommerville tetrahedra [40]; all the tetrahedra are congruent, and the face of each tetrahedron is an isosceles triangle. The unit cell vertices are

$$\mathbf{a}_1 = [0, 0, 0]^T \qquad \mathbf{a}_5 = [0, 0, \Delta z]^T$$
$$\mathbf{a}_2 = [2\Delta x, 0, \Delta z]^T \qquad \mathbf{a}_6 = [2\Delta x, 0, 4\Delta z]^T$$
$$\mathbf{a}_3 = [3\Delta x, \Delta y, 3\Delta z]^T \qquad \mathbf{a}_7 = [3\Delta x, \Delta y, 5\Delta z]^T$$
$$\mathbf{a}_4 = [\Delta x, \Delta y, 2\Delta z]^T \qquad \mathbf{a}_8 = [\Delta x, \Delta y, 6\Delta z]^T,$$

where $\Delta x = \frac{1}{6}2^{5/6}\sqrt{3}$, $\Delta y = \frac{1}{2}2^{5/6}$, and $\Delta z = \frac{1}{6}\sqrt[3]{2}\sqrt{3}$. The scaling of the vertices was chosen to give the unit cell a unit volume so that the mesh densities of the Sommerville-tetrahedral mesh and the right-tetrahedral mesh are the same.

2.2. *Dispersion Accuracy for the Yee Scheme*

The standard Yee finite-difference scheme for the Maxwell system [48] can be used as a benchmark for a tetrahedral mesh based on cubes. This scheme must be applied on a rectilinear grid, on which it is known to be second-order accurate [34], and to have the semi-discrete dispersion relation

$$\left(\omega_h^{Yee} h\right)^2 = 2\sqrt{\sin(\xi_1/2)^2 + \sin(\xi_2/2)^2 + \sin(\xi_3/2)^2}, \tag{2.1}$$

where $\xi = \mathbf{k}h$ and h is the length of the edges of the cubes in the spatial grid. The fully discrete scheme uses staggered leapfrog time stepping and has the discrete dispersion relation

$$\omega_{h,\Delta t}^{Yee} h = \frac{2}{\lambda}\sin^{-1}\left(\frac{\lambda}{2}\omega_h^{Yee} h\right),$$

where the time step is Δt and the Courant number is $\lambda = \Delta t/h$. It is apparent that the stability condition for this method is $\lambda \le 1/\sqrt{3}$ and, by analyzing the Taylor series for $\omega_{h,\Delta t}^{Yee}$ in h and Δt, one can show that the optimal choice is $\lambda = 1/\sqrt{3}$.

2.3. *Dispersion Accuracy on Cubic and Sommerville Meshes*

The general approach taken is a straightforward, albeit tedious, extension of that described in two dimensions in [29] and only the overall results of the analysis are stated here.

- For the semi-discrete edge scheme (1.6), assembling the equations for each degree of freedom for the unit cell and applying the translation property (2.1) leads to seven nontrivial discrete dispersion relations. Only one of these is the "physical" dispersion relation, converging to $\omega^2 = |\mathbf{k}|^2$ as h or equivalently $|\xi|$ is decreased. The other values for ω_h^2 are termed "parasitic" and are proportional to h^{-2}, thus having an infinite phase velocity in the limit as h tends to zero. They are similar to Bloch modes and do not seem to cause any problems in practice, but must be taken into account when the stability of the fully discrete scheme is analysed on an infinite domain.
- For the case of the semi-discrete vertex scheme (1.8), there are only three nontrivial discrete dispersion relations, as in the exact case, and hence no parasitic modes. It can be shown (using MAPLE) that on some grids (but not those used here) the node-based scheme (1.8) has the dispersion relations $\omega_h = 0$ or $\omega_h = \pm|\mathbf{k}| + O(h^4)$.

It is not possible in general to produce analytic dispersion relations for these discrete sets of equations; however, they can be computed and plotted. We display the fractional error in the phase velocity, defined as

$$e_v(\xi) = \left(\frac{\omega_h(\xi)h}{|\xi|} - 1\right), \tag{2.2}$$

where the exact phase velocity is unity.

Figures 2a to 2e show a comparison of the phase-velocity error in the Yee, edge, and vertex schemes as a function of the number of elements per wavelength along selected directions. The rate of convergence of the discrete dispersion relations for the Yee and edge schemes is roughly $O((kh)^2)$. The vertex scheme, shown in Figs. 2c and 2e, has a visibly different curvature, and both curves are consistent with an $O((kh)^4)$ convergence rate. The

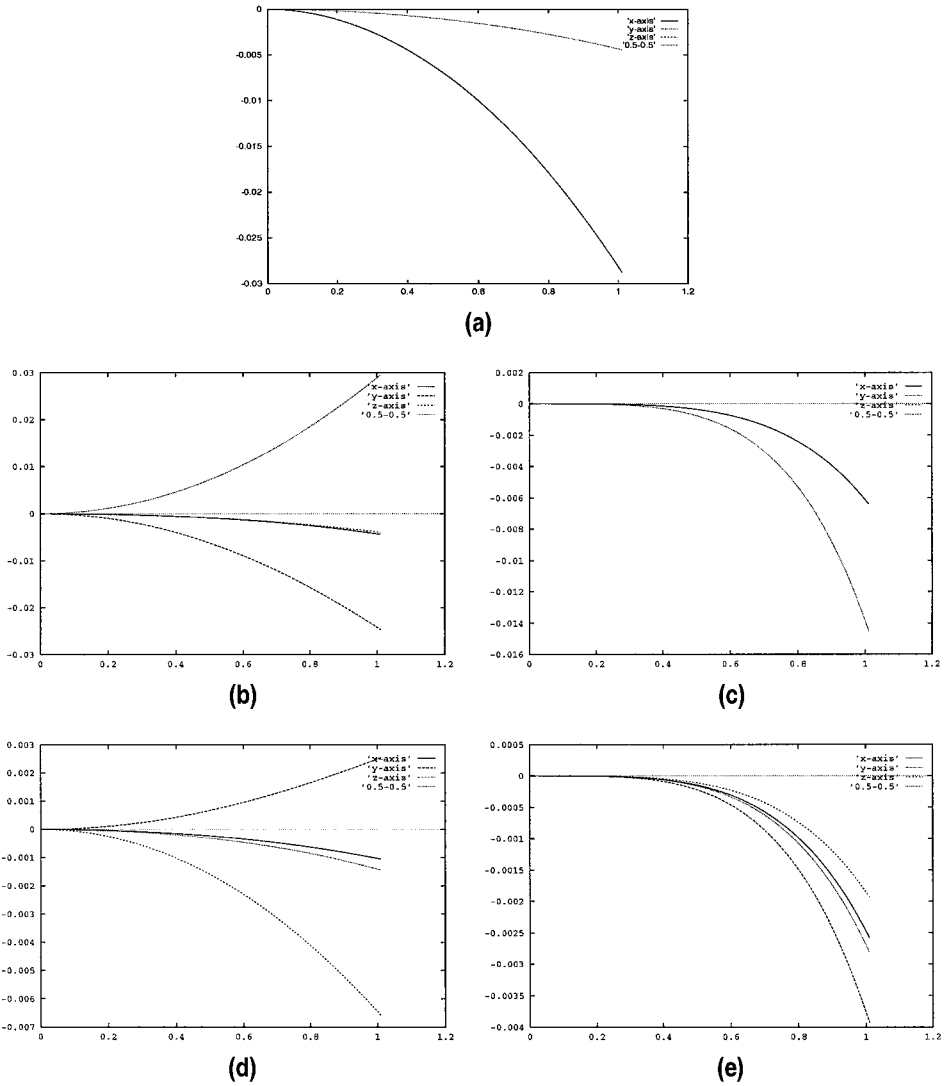

FIG. 2. Fractional phase-velocity error vs $|\xi| = |kh|$ for the cuboid and Sommerville meshes. The phase errors have been plotted along each of the three coordinate axes and along a "central" direction $\theta = \phi = 0.5$. The propagation angles θ and ϕ are defined by $k_1 = |k|\cos(\theta)\cos(\phi)$, $k_2 = |k|\sin(\theta)$, $k_3 = |k|\cos(\theta)\sin(\phi)$. Note that 10 elements per wavelength corresponds to $|\xi| = 2\pi/10 \approx 0.6$. (a) Yee scheme with cubic mesh; (b) edge elements with cubic mesh; (c) vertex scheme with cubic mesh; (d) edge elements with sommerville mesh; (e) vertex elements with sommerville mesh.

vertex results on the Sommerville meshes are better than those on the cuboid mesh by almost a factor of 4. Since the error is always negative, it may be possible to compensate for it to some degree by choosing a suitable time-stepping method. In the case of the edge-element scheme, shown in Figs. 2b and 2d, we see that the phase-velocity error has also been greatly improved by the Sommerville mesh. The overall error for a given value of $|\mathbf{k}h|$ has been decreased by roughly a factor of 4. Nevertheless, the sign of the error still depends on the direction of propagation and is still $O((kh)^2)$. This change in sign makes it impossible to compensate for this error by using a suitable time stepping scheme (as is done in the case of the Yee scheme).

Figure 3 shows a comparison of contour maps of the phase-velocity errors for the three schemes, where $e_v(\xi)$ has been plotted as a function of propagation angle. The maps identify the anisotropic character of the edge scheme, where the sign of the phase velocity error can be positive or negative depending on the direction of propagation. Inspection of the maximum phase-velocity errors in Fig. 3 shows that the vertex scheme is easily the most accurate on a given grid.

Figure 4 shows the directional characteristics of the phase-velocity error by plotting the isosurfaces $|e_v| = 1 \times 10^{-3}$ as a function of $\mathbf{k}h \in [-1, 1]^3$. The phase error for the edge scheme is highly anisotropic compared to that for the vertex scheme, and the phase error for the vertex scheme is much more isotropic on the Sommerville grid than on the cuboid grid.

Although the phase errors for these three schemes seem reasonably comparable, it should be noted that on a given cuboid mesh there are over twice as many unknowns in the edge scheme as there are in the Yee or node-based schemes. This can be seen from a direct calculation of the number of edges and vertices. On a $N \times N \times N$ grid of cubes, each decomposed into six tetrahedra, there are $3N^3 + N^2$ unknowns for the Yee or node-based scheme, while there are $7N^3 + O(N^2)$ degrees of freedom for the edge scheme. This means that for a given density of degrees of freedom (rather than tetrahedra), the edge scheme will have a much poorer phase error than the Yee scheme.

3. NUMERICAL WAVE PROPAGATION ON TETRAHEDRAL MESHES

The dispersion analysis just described is limited to regular meshes; since practical examples (e.g., the scattering example in the next section) are always non-uniform, we have carried out a number of numerical comparisons to obtain greater insight on the relative merits of the methods, using both regular meshes and partially randomized meshes. These numerical comparisons are solely concerned with the propagation accuracy; their cumulative accuracy on scattering calculations will be described in Section 4. Before presenting the numerical results the time discretisation of the semidiscrete schemes (1.6) and (1.8) needs some discussion.

3.1. *Time Discretization*

3.1.1. Edge elements. The spatially staggered nature of the degrees of freedom has led to the use of a staggered-leapfrog time discretisation with this method; applying this to the semi-discrete equations (1.6) leads to

$$\left(\epsilon\left(\mathbf{E}_h^{n+1} - \mathbf{E}_h^n\right), \psi_h\right) - \Delta t\left(\mathbf{H}_h^{n+(1/2)}, \nabla \times \psi_h\right) = -\left\langle \mathbf{H}_h^{n+(1/2)} \times \nu, \psi_h \right\rangle, \quad (3.1a)$$

$$\left(\mu\left(\mathbf{H}_h^{n+(1/2)} - \mathbf{H}_h^{n-(1/2)}\right), \phi_h\right) + \Delta t\left(\nabla \times \mathbf{E}_h^n, \phi_h\right) = 0. \quad (3.1b)$$

The resulting algebraic system can be solved by a diagonally preconditioned conjugate gradient method (see, e.g., [24]). See the Appendix for details on the convergence rates for CG and the choice of stable time step for both the edge and vertex methods.

3.1.2. The time-discrete vertex equations. The obvious choice of time discretisation for the vertex method is the Taylor–Galerkin method of Donea [15]; this is based on a Taylor

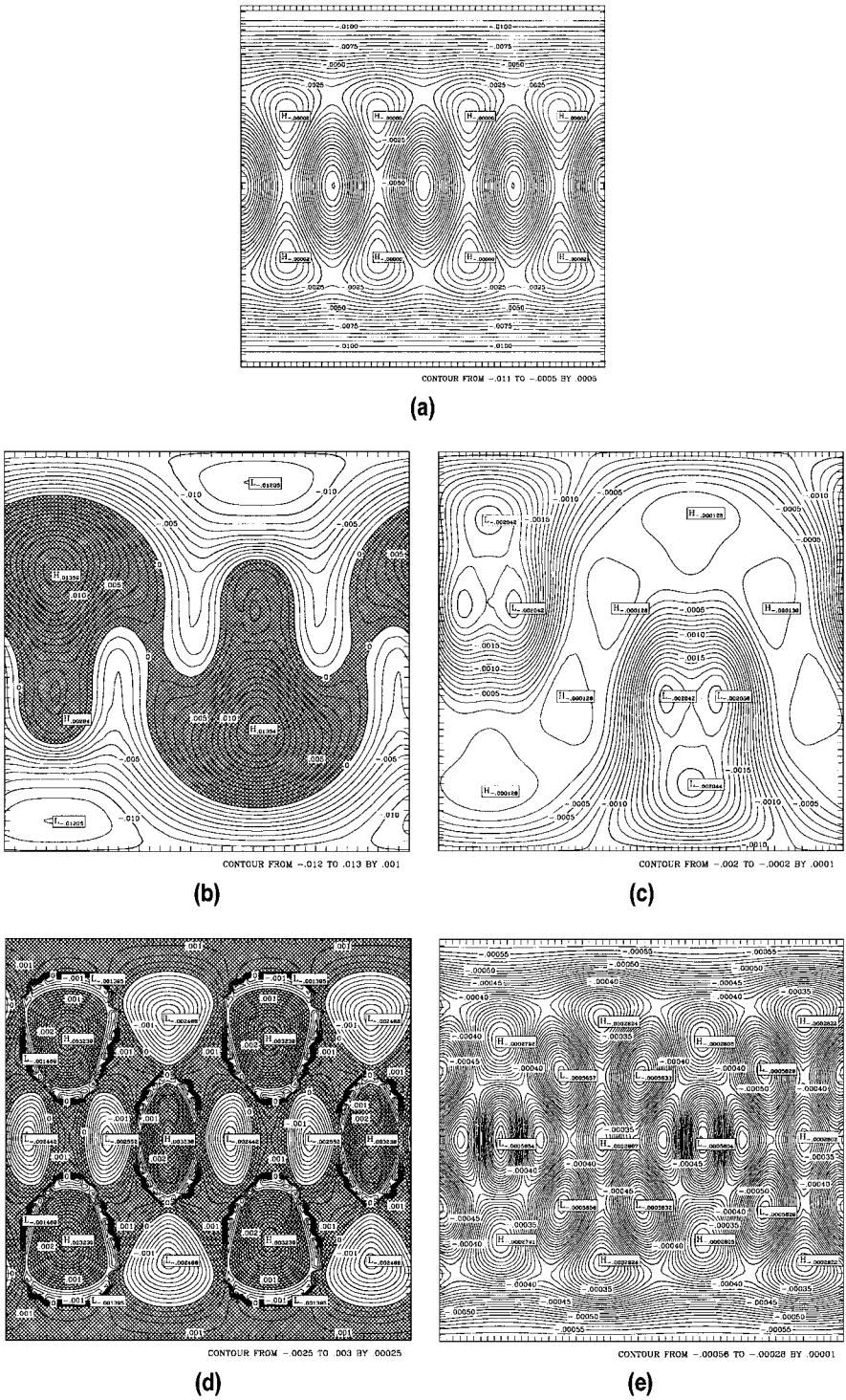

FIG. 3. *Directional maps of the fractional phase-velocity errors at 10 elements per wavelength.* The axes are the propagation angles θ and ϕ so that, e.g., $\theta = \phi = 0$ corresponds to waves travelling along the x_1 axis. The hatched areas show where the error is positive; maxima (H) and minima (L) are shown where they occur. (a) Yee scheme with cubic mesh; (b) edge elements with cubic mesh; (c) vertex scheme with cubic mesh; (d) edge scheme with Sommerville mesh; (e) Vertex scheme with sommerville mesh.

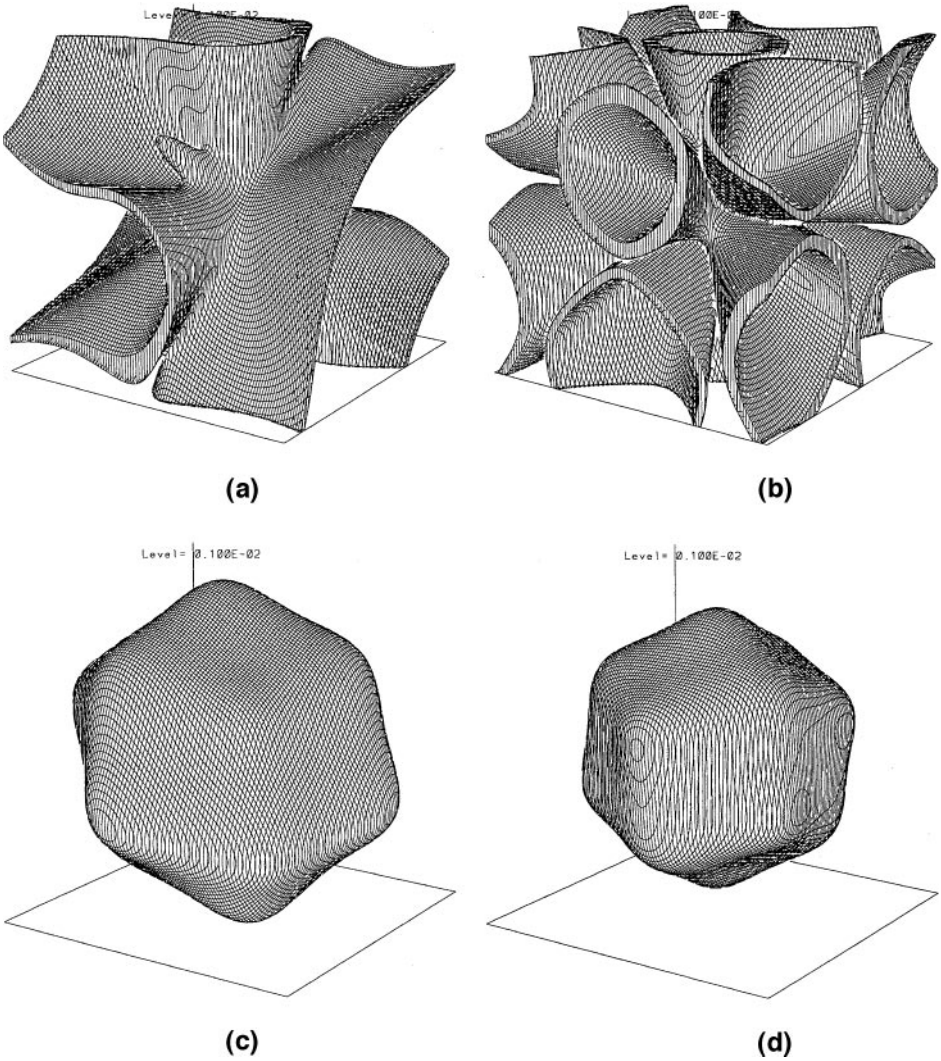

FIG. 4. *Isosurfaces of the fractional error in the phase velocity*. The isosurface chosen is for $e_v = 1 \times 10^{-3}$, and we show the region $[-1, 1] \times [-1, 1] \times [-1, 1]$ in kh space. The Sommerville mesh gives a more symmetric error in both cases. (a) Edge elements on the cuboid mesh; (b) edge elements on the Sommerville mesh; (c) vertex elements on the cuboid mesh; (d) vertex elements on the Sommerville mesh.

series expansion on the analytic fields at time $t_{n+1} = t_n + \Delta t$, namely,

$$\mathbf{E}(t_{n+1}) \approx \mathbf{E}(t_n) + \Delta t \left(\frac{\partial \mathbf{E}}{\partial t}\right)_{t_n} + \frac{1}{2}(\Delta t)^2 \left(\frac{\partial^2 \mathbf{E}}{\partial t^2}\right)_{t_n} + O(\Delta t^3),$$

where from Maxwell's equations (for constant μ, ϵ) we have that

$$\frac{\partial^2 \mathbf{E}}{\partial t^2} = -(1/\mu\epsilon)\nabla \times \nabla \times \mathbf{E} = (1/\mu\epsilon)\nabla^2 \mathbf{E},$$

using the fact that $\nabla \cdot \mathbf{E} = 0$. Since the approximate fields do not have zero divergence, the first expression is used to derive the second-order accurate time-derivative expression,

$$\left(\mathbf{E}_h^{n+1} - \mathbf{E}_h^n\right)/\Delta t + \frac{1}{2}(\Delta t/\mu\epsilon)\nabla \times \nabla \times \mathbf{E}_h^n \approx \left(\frac{\partial \mathbf{E}_h}{\partial t}\right)_{t_n} + O(\Delta t^2) \tag{3.2}$$

$$\left(\mathbf{H}_h^{n+1} - \mathbf{H}_h^n\right)/\Delta t + \frac{1}{2}(\Delta t/\mu\epsilon)\nabla \times \nabla \times \mathbf{H}_h^n \approx \left(\frac{\partial \mathbf{H}_h}{\partial t}\right)_{t_n} + O(\Delta t^2). \tag{3.3}$$

Substituting these time-derivative approximations into the semidiscrete equations (1.8), we obtain

$$\left(\epsilon \frac{\left(\mathbf{E}_h^{n+1} - \mathbf{E}_h^n\right)}{\Delta t}, \varphi_h\right) - \left(\nabla \times \mathbf{H}_h^n, \varphi_h\right) = -\frac{1}{2}\Delta t\left(\mu^{-1}\nabla \times \mathbf{E}_h^n, \nabla \times \varphi_h\right) \tag{3.4a}$$

$$\left(\mu \frac{\left(\mathbf{H}_h^{n+1} - \mathbf{H}_h^n\right)}{\Delta t}, \varphi_h\right) + \left(\nabla \times \mathbf{E}_h^n, \varphi_h\right) = -\frac{1}{2}\Delta t\left(\epsilon^{-1}\nabla \times \mathbf{H}_h^n, \nabla \times \varphi_h\right), \tag{3.4b}$$

where the $O(\Delta t^2)$ surface integrals resulting from the integration by parts of the *curl-squared terms* have been discarded.

3.2. *Numerical Results for Wave Propagation*

The numerical experiments described below are for plane-wave propagation through a cube-shaped region, which has been meshed by tetrahedra; two cases are considered:

(i) uniform right tetrahedra obtained as in Fig. 1a, from a starting mesh of $N \times N \times N$ cubic cells;

(ii) a partially randomised version of (i) obtained by randomly displacing the coordinates of each mesh point by a distance at most $0.08(2/N)$ in the x, y, and z directions.

A comparison is made between the edge-element combinations (1.4) and (1.5), the vertex element (1.7), and (on the uniform mesh) the Yee scheme on the underlying cubic lattice. The previous section showed right tetrahedra to give much poorer performance than Sommerville tetrahedra; consequently the comparison gives the Yee scheme a considerable advantage. The random mesh is also a demanding choice for the finite-element methods since an automatic mesh generator would generate smoothly varying tetrahedra. For the Yee scheme the time step is chosen to be the optimal step (the maximum step consistent with stability). The time step Δt for the vertex method is chosen to be $1/8$ the length of the shortest edge in the mesh (this is by no means maximal), and for the edge scheme the time step is the one computed using the local analysis outlined in the Appendix (but decreased, if necessary, so that $t = 3$ is an integer multiple of the time step).

The test problem is the propagation of a smooth Gaussian wave given by

$$\mathbf{E} = \mathbf{E}_0 g(\mathbf{k} \cdot \mathbf{x} - t) \quad \text{and} \quad \mathbf{H} = \mathbf{H}_0 g(\mathbf{k} \cdot \mathbf{x} - t),$$

where $g(t) = \exp(-10(s-1)^2)$ for $0 \le t \le 2$ and is zero otherwise, and $\mathbf{k} = (\cos(\theta)\cos(\phi), \sin(\theta), \cos(\theta)\sin(\phi))$, where $\theta = \phi = 0.5$ (the Yee scheme had exact propagation

in the co-ordinate directions). The polarisation of the wave is

$$\mathbf{E}_0 = (-\sin(\theta)\cos(\phi), \cos(\theta), -\sin(\theta)\sin(\phi))$$
$$\mathbf{H}_0 = (-\sin(\phi), 0, \cos(\phi)),$$

and for this simple wave-propagation problem the boundary data are given by the exact solution.

To obtain a quantitative comparison of the error in the various schemes, we shall display plots of the discrete relative L^2 error as a function of the number of degrees of freedom in the problem (number of unknowns). The following discrete L^2 error can be defined for each scheme,

$$\frac{\left(\left\|\pi_h^E \mathbf{E}(t) - \mathbf{E}_h(t)\right\|^2 + \left\|\pi_h^H \mathbf{H}(t) - \mathbf{H}_h(t)\right\|^2\right)^{1/2}}{\left(\left\|\pi_h^E \mathbf{E}(t)\right\|^2 + \left\|\pi_h^H \mathbf{H}(t)\right\|^2\right)^{1/2}}, \tag{3.5}$$

where π_h^E and π_h^H are the appropriate projection operators for the electric and magnetic field spaces for a given scheme. The error is evaluated when the wave has traversed approximately 85% of the cube diagonal. The discrete maximum error for each method is also computed. This can be formulated in the same way as (3.5); however, since the basis functions are linear, this discrete maximum norm is the same as evaluating the relative maximum error at the degrees of freedom. Comparing the numerical solution with the appropriate projection of the true solution is necessary to obtain a proper assessment of the edge-element scheme as the solution is much more accurate at the locations of the degrees of freedom than elsewhere, as is clearly visible in Fig. 5. A conventional L_2 error would simply show the $O(h)$ interpolation accuracy of the basis functions.

The uniform mesh results are shown in Fig. 6a and 6b, where the error is plotted against the number of degrees of freedom of each method rather than the mesh size. The initial slope of the lines in Fig. 6a is consistent with an error proportional to $O(h^2)$ for all methods, but on finer grids the convergence rate is more consistent with $O(h^{3/2})$ for the edge and vertex methods. In this case the Yee scheme is the most accurate and the edge scheme the least accurate method, despite the superconvergence effects at the degree-of-freedom locations. This superior performance of the Yee scheme is to be expected on uniform meshes but

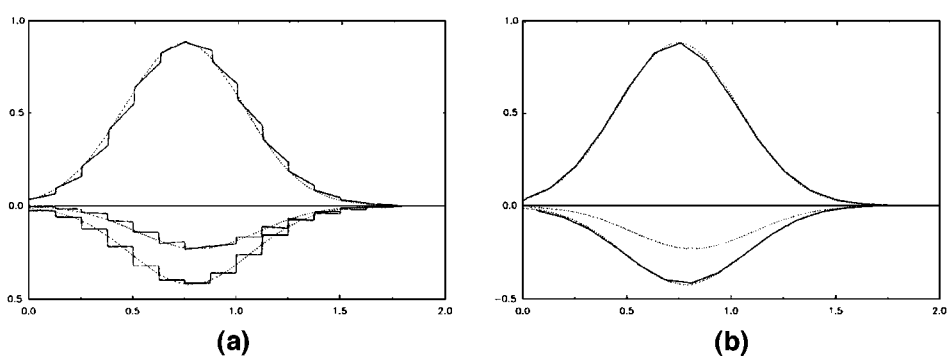

FIG. 5. Basis function representation of three components of the edge-element electric field at $t = 2.5$ and $N = 16$ on the uniform cuboid-based mesh; (a) shows the finite-element function along the line $x = y = 1$ and (b) shows an improved reconstruction by linear interpolation of edge midpoint values.

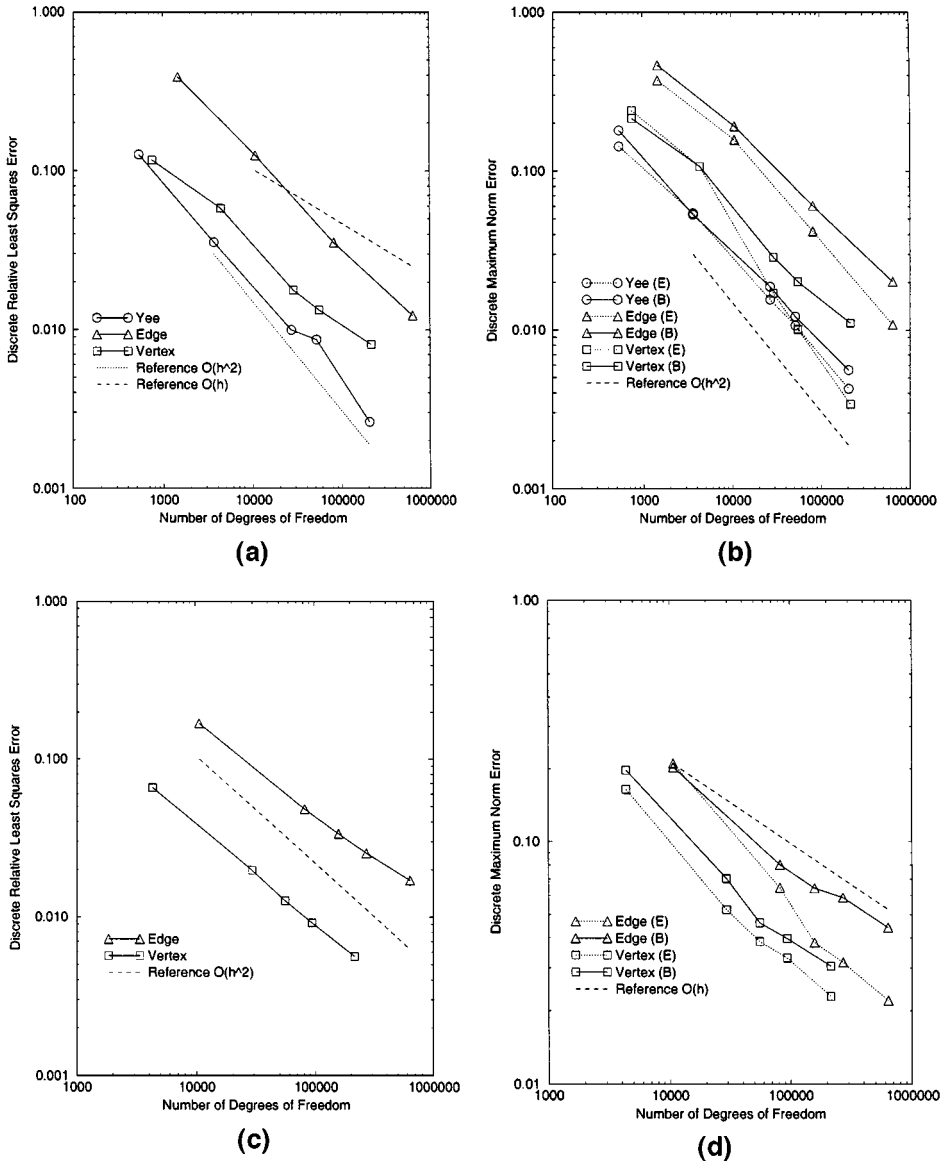

FIG. 6. Discrete L^2 error on uniform (a) and randomized (c) meshes, and the discrete maximum norm error on uniform (b) and randomized (d) meshes, plotted against the total number of degrees of freedom. Results are shown for the edge and vertex schemes, together with sight lines corresponding to $O(h)$ and $O(h^2)$ rates of convergence.

serves to confirm that finite element methods are only justified when geometric flexibility is required. Fig. 6b shows that in the maximum norm all the methods are approximately second order; however, overall, the Yee scheme is still the most accurate. Interestingly, the magnetic field computed by the edge or vertex schemes is substantially less accurate than the corresponding electric field. It appears that the error in the magnetic field accounts for the slight slowing of convergence evident in Fig. 6a.

The discrete least-squares errors for the edge and vertex schemes on the randomised mesh are shown in Fig. 6c. The vertex and edge schemes are converging at $O(h^2)$ on the coarse

grids but the rate of convergence may be slowing down on the finer grids. Nevertheless, the edge scheme is still converging faster than $O(h)$, so super-convergence of the method at the degrees of freedom seems to be insensitive to the grid perturbation we have used. The error in the edge scheme is roughly 4.5 times the error in the vertex scheme for a given number of degrees of freedom.

The discrete maximum norm error plots for the randomised mesh are shown in Fig. 6d and show that in this norm both methods are converging at $O(h)$ (compared to $O(h^2)$ on the uniform mesh). This is not necessarily inconsistent with the least-squares error results in Fig. 6c, since it is possible that there is considerable error (maybe associated with "poor" tetrahedra) but that this error is confined to small volumes in the mesh. As in the case of the uniform grid, the electric field is approximated better than the magnetic intensity (particularly for the edge scheme where the electric field is almost converging to second order).

4. SCATTERING FROM A SPHERE USING TETRAHEDRAL MESHES

This section describes the calculation of the broadband radar cross section of a perfectly conducting sphere using both vertex and edge elements. This is a more realistic setting in which to compare methods, although reference to the exact Mie solution is complicated by the use of approximate absorbing boundary conditions and polygonal approximations to the spherical surface. The comparisons are necessarily qualitative but show that accurate results can be obtained and that the accuracy is significantly affected by the choice of excitation boundary condition and by the method used for recovering the far fields. The vertex method is successful for this problem because the scatterer is smooth and convex.

Let Ω be a sufficiently smooth region with $\Omega = \Omega_1 \cup \Omega_2$ as shown in Fig. 7. A scattered-field formulation was adopted for this exterior scattering problem. Since Maxwell's

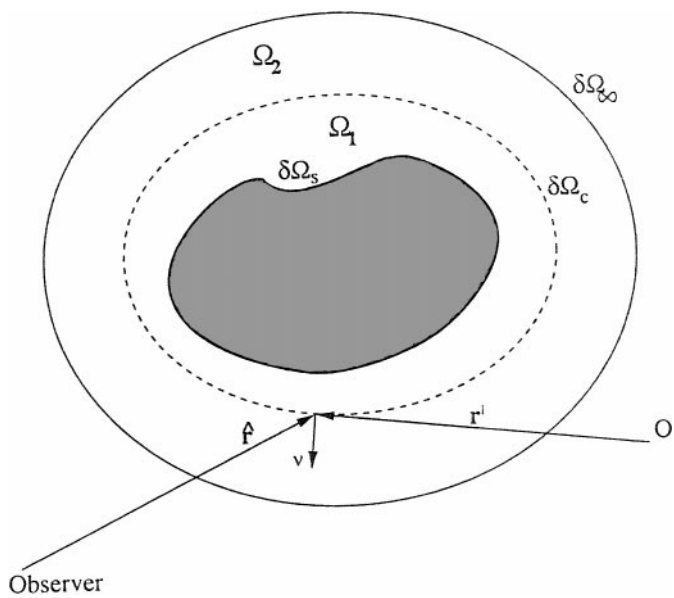

FIG. 7. The scatterer (with boundary $\partial\Omega_s$) occupies the shaded region.

equations (1.1) apply directly to the scattered fields, we simply need to provide boundary conditions on the surface of the scatterer $\partial\Omega_s$ and on the artificial truncation boundary $\partial\Omega_\infty$. The conditions used are

$$\mathbf{E} \times \nu = -\mathbf{E}_{inc} \times \nu \qquad \forall \mathbf{x} \in \partial\Omega_s, \tag{4.1a}$$

$$\mathbf{H} \times \nu = \sqrt{\epsilon/\mu}\mathbf{E}_T \qquad \forall \mathbf{x} \in \partial\Omega_\infty, \tag{4.1b}$$

where $\mathbf{E}$ and $\mathbf{H}$ now refer to the scattered electric and magnetic fields, $\mathbf{E}_{inc}$ is the known incident electric field, $\mathbf{E}_T = \nu \times (\mathbf{E} \times \nu)$ is the tangential electric field, and ν is the unit outward normal. In addition, the initial scattered fields $\mathbf{H}(\mathbf{x}, 0)$ and $\mathbf{E}(\mathbf{x}, 0)$ must be given (in our case $\mathbf{H}(\mathbf{x}, 0) = \mathbf{E}(\mathbf{x}, 0) = 0$). The Silver–Muller condition (4.1b) on $\partial\Omega_\infty$ could also have been imposed as

$$\mathbf{E} \times \nu = -\sqrt{\mu/\epsilon}\mathbf{H}_T, \tag{4.2}$$

where $\mathbf{H}_T = \nu \times (\mathbf{H} \times \nu)$ is the tangential magnetic field. Applying the Silver–Muller conditions at a finite distance from the scatterer results in an approximate absorbing boundary condition which is exact for outgoing spherical waves.

4.1. *Absorbing Boundary Conditions*

4.1.1. Edge elements. The excitation boundary condition (4.1a) can be imposed strongly with edge-element basis functions (1.4), i.e.,

$$\mathbf{E}_h \times \nu = -\left(\pi_h^E \mathbf{E}_{inc}\right) \times \nu \quad \forall \mathbf{x} \in \partial\Omega_s^h, \tag{4.3}$$

in terms of a projection of the incident field. A space of test functions with zero components along boundary edges can also be easily constructed:

$$\psi = \psi_h \in U_0^h = \{\psi_h \mid \psi_h \times \nu = 0, \forall \mathbf{x} \in \partial\Omega_s\}.$$

Using these test functions $\psi_h \in U_0^h$ with the semi-discrete equations (1.6), and imposing the absorbing boundary condition (4.1b) weakly (see [44] for a frequency domain formulation) leads to time-discrete edge-element scattering equations similarly to (3.1),

$$\epsilon\left(\frac{\mathbf{E}_h^{n+1} - \mathbf{E}_h^n}{\Delta t}, \psi_h\right) - \left(\mathbf{H}_h^{n+(1/2)}, \nabla \times \psi_h\right) = -\sqrt{\frac{\epsilon}{4\mu}}\left\langle \mathbf{E}_{hT}^n + \mathbf{E}_{hT}^{n+1}, \psi_h \right\rangle_{\partial\Omega_\infty} \tag{4.4a}$$

$$\mu\left(\frac{\mathbf{H}_h^{n+(1/2)} - \mathbf{H}_h^{n-(1/2)}}{\Delta t}, \phi_h\right) + \left(\nabla \times \mathbf{E}_h^n, \phi_h\right) = 0. \tag{4.4b}$$

If the n_e edge degrees of freedom on $\partial\Omega_s$ are numbered last, then the corresponding algebraic system can be written as

$$M_\epsilon(\mathcal{E}^{n+1} - \mathcal{E}^n) + \frac{1}{2}\Delta t M'_\epsilon(\mathcal{E}^{n+1} + \mathcal{E}^n) = \Delta t C \mathcal{H}^{n+(1/2)} \tag{4.5a}$$

$$M_\mu\left(\mathcal{H}^{n+(1/2)} - \mathcal{H}^{n-(1/2)}\right) = -\Delta t C^T \bar{\mathcal{E}}^n, \tag{4.5b}$$

where

- the vectors of electric and magnetic degrees of freedom are $\mathcal{E} = (E_1, \ldots, E_{N_e - n_e})^T$, and $\mathcal{H}^{n+(1/2)} = (H_1^{n+(1/2)}, \ldots, H_{N_f}^{n+(1/2)})^T$, $\mathcal{E} = (E_1, \ldots, E_{N_e})^T$,
- M_ϵ, $M'_\epsilon \in \mathbf{R}^{N_e - n_e \times N_e - n_e}$ are the edge mass matrix and the outer surface mass matrix, respectively,
- $M_\mu \in \mathbf{R}^{N_f \times N_f}$ is the (diagonalisable) magnetic field mass matrix,
- $C \in \mathbf{R}^{N_e \times N_f}$ is the curl matrix.

The surface mass matrix M'_ϵ can be assembled and combined with the standard mass matrix M_ϵ and the resulting system can be solved (see the Appendix) at each time step by a diagonally preconditioned conjugate gradient method [24]). An efficient parallel implementation is described in [30].

4.1.2. Vertex elements. For vertex elements, tangential boundary conditions of the form (4.3) are awkward to impose strongly because of the Cartesian form of the basis functions (1.7).

We applied integration by parts to the *curl* term in (1.8a) to allow both boundary conditions (4.1a) and (4.1b) to be imposed weakly in a manner similar to the Silver–Muller condition in (4.4a) and applied the same procedure to the **H** equations utilising (4.2). The time-discrete vertex-element equations for the scattering problem are then (following (3.4))

$$\left(\epsilon \frac{\left(\mathbf{E}_h^{n+1} - \mathbf{E}_h^n\right)}{\Delta t}, \varphi_h\right) - \left(\mathbf{H}_h^n, \nabla \times \varphi_h\right) = -\left\langle \mathbf{H}_h^n \times \nu, \varphi_h \right\rangle_{\partial\Omega_s} - \left\langle \sqrt{\epsilon/\mu}\mathbf{E}_{hT}^n, \varphi_h \right\rangle_{\partial\Omega_\infty} - \frac{1}{2}\Delta t \left(\mu^{-1}\nabla \times \mathbf{E}_h^n, \nabla \times \varphi_h\right), \tag{4.6a}$$

$$\left(\mu \frac{\left(\mathbf{H}_h^{n+1} - \mathbf{H}_h^n\right)}{\Delta t}, \varphi_h\right) + \left(\mathbf{E}_h, \nabla \times \varphi_h\right) = -\left\langle \mathbf{E}_{inc} \times \nu, \varphi_h \right\rangle_{\partial\Omega_s} - \left\langle \sqrt{\mu/\epsilon}\mathbf{H}_{hT}^n, \varphi_h \right\rangle_{\partial\Omega_\infty} - \frac{1}{2}\Delta t \left(\epsilon^{-1}\nabla \times \mathbf{H}_h^n, \nabla \times \varphi_h\right). \tag{4.6b}$$

Denoting the vectors of electric and magnetic degrees of freedom for this case as $\mathcal{E}, \mathcal{H} \in \mathbf{R}^{3N_v}$, this can be written as the following matrix problems for each time step Δt, where M_ϵ, M_μ, C, D_ϵ, $D_\mu \in \mathbf{R}^{3N_v \times 3N_v}$ are the electric and magnetic field mass matrices, the curl matrix, and the curl-squared matrices, respectively; note that the mass matrices are block diagonal, with blocks corresponding to each of the three Cartesian components. The matrix problems are

$$M_\epsilon(\mathcal{E}^{n+1} - \mathcal{E}^n) = \Delta t \left[C\mathcal{H}^n - \mathcal{G}_E^n + \frac{1}{2}\Delta t D_\mu \mathcal{E}^n\right], \tag{4.7a}$$

$$M_\mu(\mathcal{H}^{n+1} - \mathcal{H}^n) = \Delta t \left[C\mathcal{E}^n - \mathcal{G}_H^n + \frac{1}{2}\Delta t D_\epsilon \mathcal{H}^n\right], \tag{4.7b}$$

where $\mathcal{G}_E$ and $\mathcal{G}_H$ are collected surface-integral terms. These terms have been left explicit (unlike the edge case (4.5)) to avoid coupling together the surface Cartesian field components.

An interesting question arises with regard to the common practice of lumping the mass matrices M_ϵ and M_μ. The following approximation to the third-order term in the Taylor

series could be implemented (K. Morton, private communication, 1994), without adding additional complexity to the method,

$$\mathbf{E}_{ttt} \approx -(1/\mu\epsilon)\nabla^2(\mathbf{E}^{n+1} - \mathbf{E}^n)/\Delta t \tag{4.8}$$

(the Laplacian operator would be preferred in this case since it leads to a block diagonal peturbation), so that (4.7) becomes

$$\left(M_\epsilon + \frac{1}{6}\Delta t^2 L_\mu\right)(\mathcal{E}^{n+1} - \mathcal{E}^n) = \Delta t\left[C\mathcal{H}^n - \mathcal{G}_E^n + \frac{1}{2}\Delta t D_\mu \mathcal{E}^n\right], \tag{4.9a}$$

$$\left(M_\mu + \frac{1}{6}\Delta t^2 L_\epsilon\right)(\mathcal{B}^{n+1} - \mathcal{B}^n) = \Delta t\left[C\mathcal{E}^n - \mathcal{G}_H^n + \frac{1}{2}\Delta t D_\epsilon \mathcal{H}^n\right], \tag{4.9b}$$

where L_μ and L_ϵ are scaled Laplacian matrices. The peturbations clearly have a diagonalising effect on the mass matrices, and on certain regular meshes the off-diagonal terms are all negative, so there will be a choice of Δt which diagonalises all the mass matrices. Mass lumping could therefore be argued to produce an increase in the accuracy, as well as the stability, of the time discretisation. Consequently, although we have retained a consistent mass matrix in our calculations, it may be that the vertex results can be improved by mass lumping.

The excitation boundary condition (4.1a) can be imposed strongly in the vertex element method [33] despite the requirement to assign values to tangential field components. The first step is to define vertex normals and this can be done by averaging boundary-facet normals to their common vertices. A time-discrete form of Eqs. (4.6) is then solved for the field components at every vertex on the mesh. The fields at each boundary vertex are then locally resolved into normal and tangential components and the tangential components altered to match the required values. Recombining these tangential components with the unaltered normal component recovers the Cartesian component fields for the next time step. This approach has the disadvantage of introducing errors at sharp corners. The figures in Section 4.4 show a comparison of the two approaches to enforcement of these boundary conditions.

4.2. *The Radar Cross Section*

The quantity of interest is the radar cross section, a measure of the reflectivity of the scatterer. For a perfectly conducting object under plane-wave illumination, the RCS at a given frequency ω is defined as

$$\mathrm{RCS}(\omega) = \lim_{r\to+\infty} 4\pi r^2 \frac{\left|\mathbf{E}^\omega_{scat}(\mathbf{r})\right|^2}{\left|\mathbf{E}^\omega_{inc}\right|^2}, \tag{4.10}$$

where r is the distance from the observer to the scatterer, $\mathbf{E}^\omega_{scat}$ is the scattered electric field amplitude at the observer, and $\mathbf{E}^\omega_{inc}$ is the incident field amplitude at the scatterer. In general, the RCS will depend on the direction of the incident wave relative to the scatterer, though obviously not in the case of a sphere. It will also depend on the angle between the observer and the incident wave; the results in this section are for the *monostatic* RCS in which the observer direction is the same as the incident direction, i.e., reflection back in the line of sight. Because of the linearity of the problem, a time-domain method gives access (via a discrete Fourier transform of the time-varying fields) to the periodic amplitudes $\mathbf{E}^\omega$

and $\mathbf{H}^\omega$ over the range of frequencies that are excited (see [41] for a description of this technique combined with the Yee scheme). This has the advantage of allowing the RCS to be calculated over a range of frequencies in a single simulation. The pulse excitation that was used gave adequate excitation up to the highest frequencies resolvable on the available meshes.

The scattered field at infinity is recovered from the computed fields on a convex collection surface $\partial\Omega_c \in \Omega^h$ surrounding $\partial\Omega_s$, using the standard asymptotic approximation [13] (see Fig. 7 for orientation details).

$$\mathbf{E}^\omega(\mathbf{r}) = \frac{e^{ik|r|}}{|r|}\left\{\mathbf{E}_\infty(\hat{\mathbf{r}}) + O\left(\frac{1}{|r|}\right)\right\} \qquad |r| \to \infty, \tag{4.11}$$

where the far-field patterns $\mathbf{E}_\infty$, defined on the unit sphere, are given in terms of the computed fields on $\partial\Omega_c$ by

$$\mathbf{E}_\infty(\hat{\mathbf{r}}) = \frac{ik}{4\pi}\hat{\mathbf{r}} \times \int_{\partial\Omega_c} \{\nu(r') \times \mathbf{E}^\omega(r') + [\nu(r') \times \mathbf{H}^\omega(\mathbf{r}')] \times \hat{\mathbf{r}}\} e^{-ik\hat{\mathbf{r}}.\mathbf{r}'}\, dS(r'). \tag{4.12}$$

It is not obvious how best to approximate the integrals in (4.12), and in general the results will depend both on the interpolation method adopted and on the choice of collection surface. The use of the scatterer itself is an obvious choice; however, it requires a one-sided interpolation for the tangential magnetic field contributions in the case of edge elements. An example of the use of the Yee scheme can be found in [42]; the use of a stair-stepped approximation to the sphere gives rather poor results, as would be expected.

4.3. *Flux Recovery*

Of the two surface integral contributions in (4.12), it is the latter which creates the most obvious difficulties for the edge-element method since the tangential magnetic field components are not well defined on any surface composed of faces of tetrahedra. They can be estimated by interpolation, but it would be preferable to have a robust and accurate method for recovering these quantities. The general form of the surface integral or functional required is

$$\int_{\partial\Omega_c} \nu \times \mathbf{H}_\omega \cdot \mathbf{g}\, dA, \tag{4.13}$$

and an alternative to its direct calculation is to derive an equivalent expression from the global solution.

Let $\mathbf{v}$ be a vector field which has zero tangential components on $\partial\Omega_s$, is suitably smooth in both Ω_1 and Ω_2 but discontinuous across the collection surface with a jump, in its tangential components equal to $\mathbf{g}$, and has a smooth tangential vector field on $\partial\Omega_c$; i.e.,

$$\nu \times \mathbf{v} = 0 \text{ on } \partial\Omega_s,$$
$$[\mathbf{v}_T] = \mathbf{g} \text{ on } \partial\Omega_c.$$

The electromagnetic field amplitudes $\mathbf{E}^\omega$ and $\mathbf{H}^\omega$ (taking $\mathbf{E}(x,t) = \Re\{\mathbf{E}^\omega(x)e^{i(\omega t+\alpha)}\}$) satisfy the frequency domain Maxwell equations; these can be written in weak form as

$$i\omega(\epsilon\mathbf{E}^\omega, \psi) - (\mathbf{H}^\omega, \nabla \times \psi) = \langle \nu \times \mathbf{H}^\omega, \psi\rangle, \tag{4.14a}$$

$$i\omega(\mu\mathbf{H}^\omega, \phi) + (\nabla \times \mathbf{E}^\omega, \phi) = 0. \tag{4.14b}$$

We can choose $\psi = \mathbf{v}$ in (4.14a) by restricting the domain to either Ω_1 or Ω_2; thus

$$i\omega(\epsilon\mathbf{E}^\omega, \mathbf{v})_{\Omega_1} - (\mathbf{H}^\omega, \nabla \times \mathbf{v})_{\Omega_1} = \langle \nu_1 \times \mathbf{H}^\omega, \mathbf{v}\rangle_{\partial\Omega_c}, \tag{4.15a}$$

$$i\omega(\epsilon\mathbf{E}^\omega, \mathbf{v})_{\Omega_2} - (\mathbf{H}^\omega, \nabla \times \mathbf{v})_{\Omega_2} = \langle \nu_2 \times \mathbf{H}^\omega, \mathbf{v}\rangle_{\partial\Omega_c} - \left\langle \sqrt{\epsilon/\mu}\mathbf{E}_T^\omega, \mathbf{v}\right\rangle_{\partial\Omega_\infty}, \tag{4.15b}$$

and adding these two equations gives the desired functional

$$\begin{aligned}\int_{\partial\Omega_c} (\nu_1 \times \mathbf{H}^\omega) \cdot \mathbf{g}\, dA &= \int_{\partial\Omega_c} (\nu_1 \times \mathbf{H}^\omega) \cdot [\mathbf{v}_T]\, dA \\ &= i\omega(\mathbf{E}^\omega, \mathbf{v}) - (\mathbf{H}^\omega, \nabla \times \mathbf{v}) + \left\langle \sqrt{\epsilon/\mu}\mathbf{E}_T^\omega, \mathbf{v}\right\rangle_{\partial\Omega_\infty} \\ &= a_E(\mathbf{E}^\omega, \mathbf{H}^\omega; \mathbf{v}).\end{aligned} \tag{4.16}$$

The far field (4.12) can be written as a functional by taking its dot product with any unit tangent vector $\mathbf{e}$ on the unit sphere; i.e.,

$$\begin{aligned}\mathbf{e} \cdot \mathbf{E}_\infty(\hat{\mathbf{r}}) = \frac{ik}{4\pi} \Bigg\{ &\int_{\partial\Omega_c} (\nu(\mathbf{r}') \times \mathbf{E}^\omega(\mathbf{r}')) \cdot (\mathbf{e} \times \hat{\mathbf{r}})\, e^{-ik\hat{\mathbf{r}}\cdot\mathbf{r}'}\, dA(\mathbf{r}') \\ &+ \int_{\partial\Omega_c} (\nu(\mathbf{r}') \times \mathbf{H}^\omega(\mathbf{r}')) \cdot ((\hat{\mathbf{r}} \times \mathbf{e}) \times \hat{\mathbf{r}})\, e^{-ik\hat{\mathbf{r}}\cdot\mathbf{r}'}\, dA(\mathbf{r}') \Bigg\}.\end{aligned} \tag{4.17}$$

Then direct comparison between (4.16) and (4.17) shows that by taking

$$[\mathbf{v}_T] = \mathbf{g} = ((\hat{\mathbf{r}} \times \mathbf{e}) \times \hat{\mathbf{r}}) e^{-ik\hat{\mathbf{r}}\cdot\mathbf{r}'} \tag{4.18}$$

the functional can be rewritten so that the surface integral terms depending on the tangential magnetic field components on $\partial\Omega_c$ are replaced by volume integral terms depending on the global solution, as required:

$$\mathbf{e} \cdot \mathbf{E}_\infty(\hat{\mathbf{r}}) = \frac{ik}{4\pi} \left\{ \int_{\partial\Omega_c} (\mathbf{e} \times \hat{\mathbf{r}}) \cdot (\nu(\mathbf{r}') \times \mathbf{E}^\omega(\mathbf{r}')) e^{-ik\hat{\mathbf{r}}\cdot\mathbf{r}'} dA + a_E(\mathbf{E}^\omega, \mathbf{H}^\omega; \mathbf{v}) \right\}. \tag{4.19}$$

The choice of three independent unit vectors $\mathbf{e}_1, \mathbf{e}_2, \mathbf{e}_3$ then allows a complete determination of $\mathbf{E}_\infty(\hat{\mathbf{r}})$ for any given $\hat{\mathbf{r}}$. Note that this definition is independent of the continuation of $\mathbf{v}$ into Ω_1 and Ω_2. To see this, suppose $\mathbf{v}_1$ and $\mathbf{v}_2$ are two choices of $\mathbf{v}$ satisfying the above jump conditions; then $\mathbf{v}_1 - \mathbf{v}_2$ is a continuous function on the whole of Ω and can be used as a test function in (4.14a); i.e., $a_E(\mathbf{E}^\omega, \mathbf{H}^\omega; \mathbf{v}_1 - \mathbf{v}_2) = 0$. Consequently we are free to choose the continuation of $\mathbf{v}$ in such a way as to minimise the extra computation created by replacing a surface integral by a volume integral. To see how to do this, assume that $\mathbf{E}_h^\omega$ and $\mathbf{H}_h^\omega$ are the edge finite-element approximate solutions to the frequency domain Maxwell's equations; then by an analogous procedure to the exact case we have that

$$\mathbf{e} \cdot \mathbf{E}_{h,\infty} = \frac{ik}{4\pi} \left\{ \int_{\partial\Omega_c} (\mathbf{e} \times \hat{\mathbf{r}}) \cdot \left(\nu(\mathbf{r}') \times \mathbf{E}_h^\omega(\mathbf{r}')\right) e^{-ik\hat{\mathbf{r}}\cdot\mathbf{r}'} dA(\mathbf{r}') + a_E\left(\mathbf{E}_h^\omega, \mathbf{H}_h^\omega; \mathbf{v}_h\right) \right\}, \tag{4.20}$$

where $\mathbf{v}_h$ is an edge finite-element function (1.4) (i.e., with tangential degrees of freedom) on Ω_1 or Ω_1, but discontinuous across $\partial\Omega_c$ such that

$$\nu \times \mathbf{v}_h = 0 \text{ on } \partial\Omega_s,$$

$$[\mathbf{v}_{h,T}] = \mathbf{g}_h \text{ on } \partial\Omega_c,$$

where

$$\mathbf{g}_h \approx (\hat{\mathbf{r}} \times \mathbf{e}) \times \hat{\mathbf{r}} e^{-ik\hat{\mathbf{r}}\cdot\mathbf{r}'}. \tag{4.21}$$

In fact we take $\mathbf{g}_h$ to be the interpolant of $(\hat{\mathbf{r}} \times \mathbf{e}) \times \hat{\mathbf{r}} e^{-ik\hat{\mathbf{r}}\cdot\mathbf{r}'}$ on $\partial\Omega_c$. A useful choice for a practical implementation of the extraction procedure is

$$\mathbf{v}_h = 0 \text{ on } \Omega_1,$$
$$\mathbf{v}_h = 0 \text{ at all interpolation points in } \Omega_2,$$

and $[\mathbf{v}_{h,T}]$ is as discussed above. In this case

$$a_E\left(\mathbf{E}_h^\omega, \mathbf{H}_h^\omega; \mathbf{v}_h\right) = \sum_{\substack{K\in\Omega_1 \\ \partial K\cap\partial\Omega_c\neq\emptyset}} \int_K \left(i\omega\left(\mathbf{E}_h^\omega \cdot \mathbf{v}_h\right) - \mathbf{H}_h^\omega \cdot \nabla \times \mathbf{v}_h\right) dV. \tag{4.22}$$

Thus the volume integral need only be performed over a thin "skin" of width $O(h)$ outside $\partial\Omega_c$. This looks rather "one sided", but is merely a convenient choice of $\mathbf{v}_h$.

These expressions require slight modification (an $O(\Delta t)^2$ peturbation) in our case since $\mathbf{E}_h^\omega$ and $\mathbf{H}_h^\omega$ are obtained from time-domain values using a discrete Fourier transform. Consequently (4.22) is replaced by

$$\tilde{a}_E\left(\mathbf{E}_h^\omega, \mathbf{H}_h^\omega; \mathbf{v}_h\right) = \sum_{\substack{K\in\Omega_1 \\ \partial K\cap\partial\Omega_c\neq\emptyset}} \int_K \left(\frac{e^{i\omega\Delta t/2} - e^{-i\omega\Delta t/2}}{\Delta t}\left(\mathbf{E}_h^\omega \cdot \mathbf{v}_h\right) - \mathbf{H}_h^\omega \cdot \nabla \times \mathbf{v}_h\right) dV. \tag{4.23}$$

This type of reformulation has been used in many other finite-element contexts in which a flux surface integral is required and can be shown to improve the asymptotic order of accuracy of the far field. The error analysis is outlined in Appendix 2, and despite the first-order accurate nature of the terms in (4.20) the far field can be shown to be second-order.

4.4. *Results*

Time-domain scattering calculations for broadband illumination of a perfectly conducting sphere were carried out using both the edge-element approximation (4.5) and the vertex-element approximation (4.7). The RCS was calculated as a function of wavelength and compared with the exact Mie series solution. For the vertex-element case the RCS was calculated as a function of wavelength by direct approximation of the complete far-field integral. The following two meshes of a conducting sphere of radius 0.25 containing domain $[-1, 1] \times [-1, 1] \times [-1, 1]$ were used:

- **Sphere 1**: $N_k \approx 70,000$, $N_e \approx 90,000$, $N_v \approx 13,000$
- **Sphere 2**: $N_k \approx 110,000$, $N_e \approx 230,000$, $\approx N_v \approx 19,000$.

It can be seen in Fig. 8 that the mesh Sphere 2 resolves the sphere significantly better than Sphere 1 by using a more refined mesh closer to the surface.

Figure 9 shows a comparison of vertex element RCS calculations for both the strong and the weak imposition of the boundary excitation (4.1a) for the finer mesh. The normalised echo area $(1/\pi a^2)$ RCS (ω) is plotted against the sphere radius in wavelengths so that reflectivity is plotted against frequency. The complete curve was obtained from a single scattering

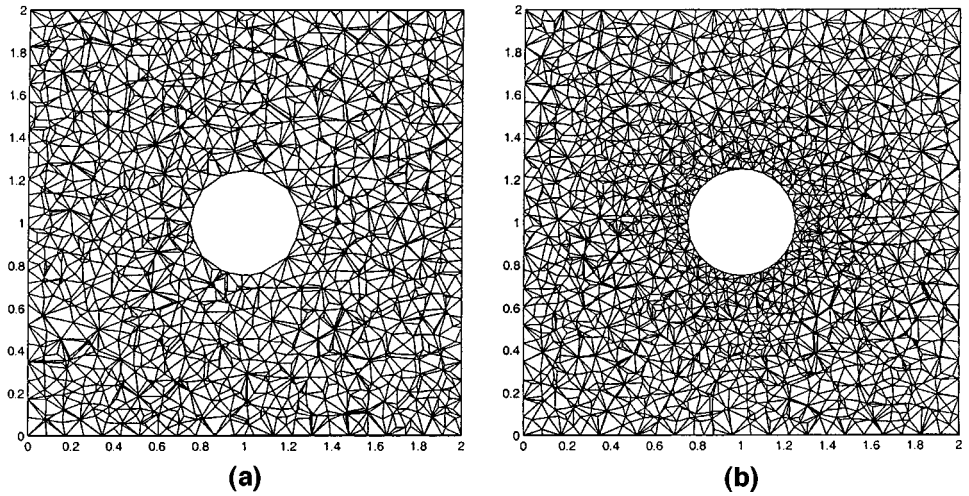

FIG. 8. Tetrahedral mesh sections indicating the geometry resolution of the meshes used in the scattering calculations. (a) sphere 1 ($N_v \approx 13{,}000$); (b) sphere 2 ($N_v \approx 19{,}000$).

calculation by discrete Fourier transform of the time varying fields over the required range of frequencies. In this case there are ≈32 elements along the sphere circumference giving approximately five elements per sphere radius. The far fields have been computed by direct approximation of (4.12) evaluated on collection surface positioned roughly halfway

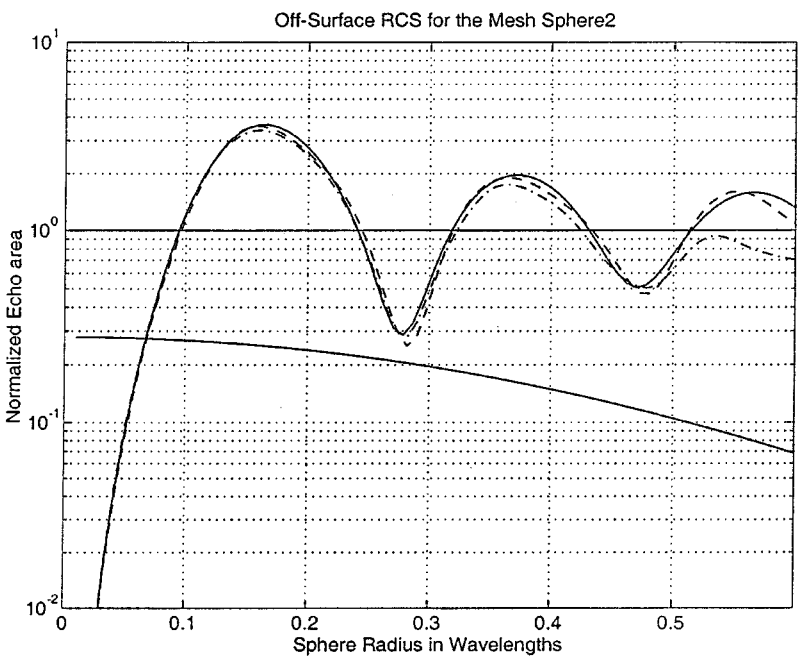

FIG. 9. Comparisons of the computed vertex element RCS for a sphere with the exact Mie series solution (solid line), comparing the weak imposition (I) of the scattering boundary conditions (dashed line) against the strong imposition (II) using averaged normals (dashed–dotted line). The lower solid line shows the energy distribution of incident Gaussian pulse.

between the sphere and the outer boundary. The variation of the backscatter coefficient with frequency is accurate to better than a decibel up to an electrical size of 0.6λ, corresponding to a resolution of 10 elements per wavelength. The results confirm that the weak imposition is superior (and is also easier and more natural to implement) with the improvement most significant at the high-frequency sampling of the time-varying fields. They also confirm the effectiveness of the weakly imposed Silver–Muller conditions for this element (they are imposed at a distance of around 1.5λ at the shortest wavelength sampled), despite its being a first-order condition.

Figure 10 shows a comparison of edge-element RCS calculations for the collection surface positioned either on the surface of the sphere itself or roughly halfway between the sphere and the outer boundary. The RCS was calculated both by direct approximation of the complete far-field integral (4.12), using one-sided estimation of $\int_{\partial\Omega_{rcs}} (\nu \times \mathbf{H}^{\omega}) \cdot \phi \, dA$, and by the new flux-recovery form (4.20). It can be seen that the use of a new far-field recovery procedure has led to more accurate results for backscatter coefficients on these meshes. This supports the assertion in Appendix B that this technique for the recovery

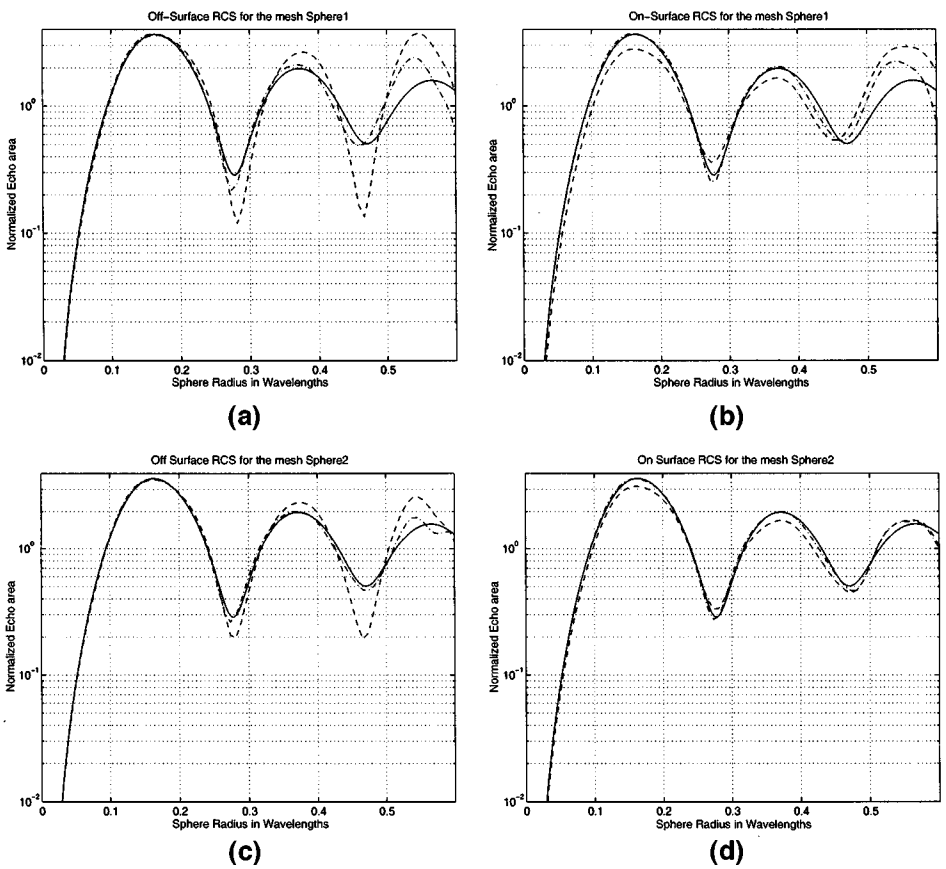

FIG. 10. Comparisons of the computed RCS using the edge-element method for the Sphere 1 and Sphere 2 meshes with the exact Mie series solution (solid line), using far fields calculated using the standard formulation (dashed line - - -), and using the flux-recovery formulation (dash–dotted line - · -). (a) Sphere 1: off-surface RCS collection surface; (b) Sphere 1: on-surface RCS collection surface; (c) Sphere 2: off-surface RCS collection surface; (d) Sphere 2: on-surface RCS collection surface.

of far fields from first-order edge-element solutions results in second-order accuracy. The on-surface recovery procedure appears to be robust, avoids the need to define collection surfaces, and provides the most accurate results.

The edge-element calculation provides accuracy comparable (with the new far-field recovery) to that of the vertex-element calculation on the same mesh. As noted earlier, the edge-element method is the more expensive calculation because of the greater number of degrees of freedom; however, the vertex method is still severely restricted in 3D to scatterers with smooth surfaces and no reentrant corners.

5. CONCLUSIONS

A 3-D dispersion analysis of the edge-element finite-element method on tetrahedral meshes has been carried out and compared with vertex elements. The analysis clearly demonstrates that the mesh character has a significant influence on phase accuracy and moreover that a "uniform" Sommerville mesh works better than right tetrahedra in both the cases. The difference is particularly pronounced for edge elements. The analysis also shows that the vertex scheme is fourth-order accurate in phase error, compared to second-order for the edge scheme.

Comparative results for numerical wave propagation demonstrate the advantage of the vertex elements, and implementation issues support this advantage. The loss of accuracy observed with partially randomised meshes is significant; however, the overall rate of convergence remains close to second order.

Results for scattering from a sphere show that, with weakly imposed boundary conditions, the vertex method is still more accurate on the same mesh and should be cheaper to compute. However, the advantage is not as pronounced as in simple wave propagation and use of a new far-field recovery procedure leads to equivalent accuracy with the edge method. The on-surface recovery procedure appears to be robust and avoids the need to define collection surfaces. These results support arguments, based on the analysis in the Appendix, for second-order accuracy for the edge-element recovered far fields.

APPENDIX A

Algebraic Properties

Although the discrete system of equations require the solution of an algebraic system at every time step, they still have a time step stability limit; in fact, the algebraic systems are well conditioned and are easily solved using a small number of diagonally preconditioned conjugate gradient iterations. The following sections develop estimates of the convergence rates for the CG iteration and of the time step restriction, based on the approach of Wathen [43].

Edge Elements

For the case of edge elements, the magnetic field mass matrix M in (4.5) can be diagonalised and hence easily solved. The electric field mass matrix M_ϵ, however, is symmetric, positive definite, and sparse (see [18] for an analysis of the sparsity pattern). Let M_ϵ^K be the mass matrix for element $K \in \Omega_h$, and let D_ϵ^K be the diagonal matrix formed from the main

diagonal of M_ϵ^K. Then the eigenvalues of the diagonally preconditioned matrix M_ϵ are real and lie in $[\lambda_l, \lambda_u]$, where $\lambda_l = \min_{K\in\Omega_h} \lambda_K^{min}$, $\lambda_u = \max_{K\in\Omega_h} \lambda_K^{max}$, and

$$\lambda_K^{min} = \min_{x\neq 0} \frac{\mathbf{x}^T M_\epsilon^K \mathbf{x}}{\mathbf{x}^T D_\epsilon^K \mathbf{x}} \quad \text{and} \quad \lambda_K^{max} = \max_{x\neq 0} \frac{\mathbf{x}^T M_\epsilon^K \mathbf{x}}{\mathbf{x}^T D_\epsilon^K \mathbf{x}}.$$

For the cuboid grid based on the unit cell shown in Fig. 1, $\lambda_u/\lambda_l = 6.433$, which implies that at each step of the preconditioned conjugate gradient algorithm, the error is decreased by a factor of approximately 0.43. For the Sommerville grid, the above analysis gives a condition number estimate of 5 and hence a convergence factor of 0.38 per conjugate gradient step.

Next we turn to the problem of choosing a stable time step. Numerical computations of ω_h on the cuboid-based grid show that $\max_{\mathbf{k}} \omega_h h \approx 8.5$ and hence the leap frog time-stepping scheme has a stability constraint of $\Delta t/h \leq 0.23$, where Δt is the time step and h is the length of the sides of the cubic mesh which underlies the tetrahedralization. For a nonuniform mesh, the stability bound is more difficult to compute, so we outline a method for computing a quick approximation to the stability bound using the methods of Wathen.

Assuming zero boundary data and applied current, eliminating the magnetic field from (4.5) gives

$$M_\epsilon(\mathcal{E}^{n+1} - 2\mathcal{E}^n + \mathcal{E}^{n+1}) + (\Delta t)^2 C^T M - \mu^{-1} C\mathcal{E}^n = 0.$$

From this it is clear that if ω_h^{max} is the largest eigenvalue of the generalized eigen problem

$$\omega_h^2 M_\epsilon \vec{V} = C^T M_\mu^{-1} C\vec{V},$$

the method is stable provided $(\Delta t)\omega_h^{max} \leq 2$. But since $\nabla \times U_h^N \subset V_h^N$ we know that $C^T M_\mu^{-1} C$ is just the matrix corresponding to the bilinear form $a(\mathbf{u}, \mathbf{v}) = (\nabla \times \mathbf{u}, \mu^{-1}\nabla \times \mathbf{v})$. Hence if S_K is the elemental matrix corresponding to the bilinear form

$$a_K(\mathbf{u}, \mathbf{v}) = \int_K \nabla \times \mathbf{u} \cdot \mu^{-1} \nabla \times \mathbf{v}\, dV$$

and if M_ϵ^K is the elemental mass matrix as before, then

$$\omega_h^{max} \leq \max_{K\in\Omega_h} \omega_K^{max},$$

where ω_K^{max} is the largest eigenvalue of the local eigenvalue problem

$$\omega_K^2 M_\epsilon^K \vec{v} = S_K \vec{v}.$$

Of course, such an estimate is likely to be rather poor if there are only a few very "poor" tetrahedra in the mesh, but we have found that it performs quite well in practice.

Vertex Elements

In this case both M_ϵ and M_μ are symmetric, positive definite, and sparse, and the Wathen bound on the condition number of the preconditioned matrix M_ϵ is 5, independent of the mesh, giving a convergence factor of 0.38 per conjugate gradient step. This indicates that conjugate-gradient method should converge faster for the node-based scheme than for the edge-based scheme, although it requires two conjugate gradient solves per time step.

APPENDIX B

Far-Field Errors

Note that

$$\mathbf{e}\cdot\mathbf{E}_\infty - \mathbf{e}\cdot\mathbf{E}_{\infty,h} = \frac{ik}{4\pi}\left\{\int_{\partial\Omega_{rcs}} (\mathbf{e}\times\hat{\mathbf{r}}\exp(-ik\hat{\mathbf{r}}\cdot\mathbf{r}'))\cdot\left(\mathbf{E}^\omega - \mathbf{E}_h^\omega\right) dA \right.$$
$$\left. + a_E(\mathbf{E}^\omega, \mathbf{H}^\omega; \mathbf{v}) - a_E\left(\mathbf{E}_h^\omega, \mathbf{H}_h^\omega; \mathbf{v}_h\right)\right\}.$$

We choose $\mathbf{v} = \mathbf{v}_h$, and let $\mathbf{z}$ be any sufficiently smooth function with a possible jump across $\partial\Omega_{rcs}$. Then

$$a_E(\mathbf{E}^\omega, \mathbf{H}^\omega; \mathbf{v}) - a_e\left(\mathbf{E}_h^\omega, \mathbf{H}_h^\omega; \mathbf{v}_h\right) = a_E\left(\mathbf{E}^\omega - \mathbf{E}_h^\omega, \mathbf{H}^\omega - \mathbf{H}_h^\omega; \mathbf{v}_h - \mathbf{z}\right)$$
$$+ a_E\left(\mathbf{E}^\omega - \mathbf{E}_h^\omega, \mathbf{H}^\omega - \mathbf{H}_h^\omega; \mathbf{z}\right).$$

We want to choose $\mathbf{z}$ so that the pair $(\mathbf{z}, \mathbf{w})$ satisfies the transmission problem

$$\begin{aligned}
-ik\mathbf{w} - \nabla\times\mathbf{z} &= 0 \text{ in } \Omega_1 \text{ and } \Omega_2,\\
-ik\mathbf{z} + \nabla\times\mathbf{w} &= 0 \text{ in } \Omega_1 \text{ and } \Omega_2,\\
\nu\times\mathbf{w} &= 0 \text{ on } \partial\Omega_s,\\
[\mathbf{w}_T] &= \mathbf{f} \text{ on } \partial\Omega_{rcs},\\
[\mathbf{z}_T] &= (\hat{\mathbf{r}}\times\mathbf{e})\times\hat{\mathbf{r}}\exp(-ik\hat{\mathbf{r}}\cdot\mathbf{r}') \text{ on } \partial\Omega_{rcs},\\
\nu\times\mathbf{w} - \mathbf{z}_T &= 0 \text{ on } \partial\Omega_{inf},
\end{aligned}$$

where $\mathbf{f}$ is as yet unspecified. For edge spaces, the magnetic equation is satisfied exactly so that

$$\mathbf{H}^\omega - \mathbf{H}_h^\omega = \frac{1}{ik}\nabla\times\left(\mathbf{E}^\omega - \mathbf{E}_h^\omega\right).$$

It can then be shown, using the boundary conditions for $\mathbf{w}$ and the jump conditions for $\mathbf{w}$ and $\mathbf{z}$ to simplify the boundary term, that

$$a_E\left(\mathbf{E}^\omega - \mathbf{E}_h^\omega, \mathbf{H}^\omega - \mathbf{H}_h^\omega; \mathbf{z}\right) = \int_{\partial\Omega_{rcs}} \nu\times\left(\mathbf{E}^\omega - \mathbf{E}_h^\omega\right)\cdot[\mathbf{w}_T]\, dA.$$

Hence

$$\mathbf{e}\cdot\mathbf{E}_\infty - \mathbf{e}\cdot\mathbf{E}_{h,\infty} = \frac{ik}{4\pi}\left\{a_E\left(\mathbf{E}^\omega - \mathbf{E}_h^\omega, \mathbf{H}^\omega - \mathbf{H}_h^\omega; \mathbf{v}_h - \mathbf{z}\right) + \int \mathbf{e}\cdot\hat{\mathbf{r}}\times\left(\nu\times\left(\mathbf{E}^\omega\right.\right.\right.$$
$$\left.\left.\left. - \mathbf{E}_h^\omega\right)\right)\exp(-ik\hat{\mathbf{r}}\cdot\mathbf{r}') + \nu\times\left(\mathbf{E}^\omega - \mathbf{E}_h^\omega\right)\cdot\mathbf{f}\, dA\right\}.$$

We can now make the choice

$$\mathbf{f}(\mathbf{r}') = -(\mathbf{e}\times\hat{\mathbf{r}})_T\exp(-ik\hat{\mathbf{r}}\cdot\mathbf{r}')$$

and obtain the estimate

$$\mathbf{e}\cdot\mathbf{E}_\infty - \mathbf{e}\cdot\mathbf{E}_{h,\infty} = \frac{ik}{4\pi} a_E\left(\mathbf{E}^\omega - \mathbf{E}_h^\omega, \mathbf{H}^\omega - \mathbf{H}_h^\omega; \mathbf{v}_h - \mathbf{z}\right)$$

which indicates that, for first-order edge elements, the method will provide second-order accuracy for the far fields. The use of the time-domain method will not change the estimates by more than $O(\Delta t^2)$.

ACKNOWLEDGMENT

Antoine LeHyaric is thanked for his work on implementing the scattering version of the vertex code and in carrying out the computations on the sphere as a part of an EPSRC/D.T.I Parallel Applications Project, project partly funded by British Aerospace.

REFERENCES

1. F. Assous, P. Ciarlet, Jr., and J. Segré, Numerical solution to the time-dependent Maxwell equations in two-dimensional singular domains: The Singular Complement Method, *J. Comput. Phys.* **161**, 218 (2000).
2. F. Assous, P. Ciarlet, Jr., and E. Sonnendrücker, Resolution of the Maxwell equations in a domain with reentrant corners, *RAIRO Model. Math. Anal. Numer.* **32**(3), 359 (1998).
3. I. Babuška and A. Miller, The post-processing approach in the finite element method. 1. Calculation of displacements, stresses and other higher derivatives of the displacements, *Int. J. Numer. Meth. Eng.* **20**, 1085 (1984).
4. I. Babuška and A. Miller, The post-processing approach in the finite element method. 2. The calculation of stress intensity factors, *Int. J. Numer. Meth. Eng.* **20**, 110 (1984).
5. I. Babuška and A. Miller, The post-processing approach in the finite element method. 3. A posteriori error estimates and adaptive mesh selection, *Int. J. Numer, Meth. Eng.* **20**, 2311 (1984).
6. M. Barton and Z. Cendes, New vector finite elements for three-dimensional magnetic computation, *J. Appl. Phys.* **61**, 3919 (1987).
7. A. Bespalov, Finite element method for the eigenmode problem of a RF cavity, *Sov. J. Numer. Anal. Math. Model.* **3**, 163 (1988).
8. A. Bossavit, Mixed finite elements and the complex of Whitney forms, in *The Mathematics of Finite Elements and Applications VI*, edited by J. Whiteman (Academic Press, San Diego, 1988), pp. 137–144.
9. A. Bossavit, The computation of eddy-currents, in dimension 3, by using mixed finite elements and boundary elements in association, *Math. Comput. Model.* **15**, 33 (1991).
10. W. Boyse, D. Lynch, K. Paulsen, and G. Minerbo, Node based finite element modelling of Maxwell's equations, *IEEE Trans Ant. Propagat.* **40**, 642 (1992).
11. A. Chatterjee, J. Jin, and J. Volakis, Edge-based finite elements and vector ABC's applied to 3D scattering, *IEEE Trans Ant. Propagat.* **41**, 221 (1993).
12. G. Cohen and P. Monk, Gauss point mass lumping schemes for Maxwell's equations, *Numer. Meth. PDEs* **14**, 63 (1998).
13. D. L. Colton and R. Kreiss, *Inverse Acoustic and Electromagnetic Scattering Theory* (Springer-Verlag, Berlin, (1993).
14. J. D'Angelo and I. Mayergoyz, Finite element methods for the solution of RF radiation and scattering problems, *Electromagnetics* **10**, 177 (1990).
15. J. Donea, Taylor-Galerkin method for convective transport problems, *Int. J. Numer. Meth. Eng.* **20**, 101 (1984).
16. F. Hermeline, Two coupled particle-finite volume methods using Delaunay–Voronoï meshes for the approximation of Vlassov–Poisson and Vlasov–Maxwell equations, *J. Comput. Phys.* **106**, 1 (1993).
17. J.-M. Jin, *The Finite Element Method in Electromagnetics* (Wiley, New York, 1993).

18. P. Kotiuga, Essential arithmetic for evaluating three dimensional vector finite element interpolation schemes, *IEEE Trans. Magnet.* **27**, 5208 (1991).
19. J. Lee, WETD—A finite element time-domain approach for solving Maxwell's equations, *IEEE Microwave Guided Wave Lett.* **4**, 11 (1994).
20. J.-F. Lee, *Solving Maxwell's Equations by Finite Element Time Domain Methods*, preprint (1993).
21. V. Levillain, Eigenvalue approximation by mixed methods for resonant inhomogeneous cavities with metallic boundaries, *Math. Comput.* **58**, 11 (1992).
22. N. Madsen and R. Ziolkowski, Numerical solution of Maxwell's equations in the time domain using irregular nonorthogonal grids, *Wave Motion* **10**, 583 (1988).
23. K. Mahadevan and R. Mittra, Radar cross section computations of inhomogeneous scatterers using edge-based finite element method in frequency and time domains, *Radio Sci.* **28**, 1181 (1993).
24. K. Mahadevan, R. Mittra, and P. M. Vaidya, Use of Whitney's edge and face elements for efficient finite element time domain solution of Maxwell's equations, *J. Electromagn. Waves Appl.* **8**, 1173 (1994).
25. B. McCartin and J. Dicello, Three dimensional finite difference frequency domain scattering computation using the control region approximation, *IEEE Trans. Mag.* **25**, 3092 (1989).
26. P. Monk, A mixed method for approximating Maxwell's equations, *SIAM J. Numer. Anal.* **28**, 1610 (1991).
27. P. Monk, An analysis of Nédélec's method for the spatial discretization of Maxwell's equations, *J. Comput. Appl. Math.* **47**, 101 (1993).
28. P. Monk, Superconvergence of finite element approximations to Maxwell's equations, *Numer. Meth. PDEs* **10**, 793 (1994).
29. P. Monk and A. K. Parrott, A dispersion analysis of finite element methods for Maxwell's equations, *SIAM J. Sci. Comput.* **15**, 916 (1994).
30. P. Monk, A. K. Parrott, and P. Wesson, A parallel electromagnetic scattering code, *COMPEL,* **13** (Supp A) (1994).
31. P. Monk, A. K. Parrott, and A. Le Hyaric, *Analysis of Finite Element Time Domain Methods in Electromagnetic Scattering,* Oxford University Computing Laboratory Report 96/25.
32. P. Monk and E. Süli, The adaptive computation of far field patterns by a posteriori error estimation of linear functionals, *SIAM J. Numer. Anal.* **36**, 274 1998.
33. K. Morgan, O. Hassan, and J. Peraire, A time domain unstructured grid approach to the stimulation of electromagnetic scattering in piecewise homogeneous media, *Comput. Meth. Appl. Mech. Eng.* **134**, 17 (1996).
34. P. Monk and E. Süli, A convergence analysis of Yee's scheme on non-uniform grids, *SIAM J. Numer. Anal.* **31**, 412 (1994).
35. K. Madhevan, R. Mittra, and P. M. Vaidya, Use of Whitney's edge and face elements for efficient finite element time domain solution of Maxwell's equations, *J. Electromagn. Waves Appl.* **8**, 1173 (1994).
36. G. Mur, The finite-element modeling of three-dimensional time-domain electromagnetic fields in strongly inhomogeneous media, *IEEE Trans. Magn.* **28**, 1130 (1992).
37. G. Mur and A. de Hoop, A finite-element method for computing three-dimensional electromagnetic fields in inhomogeneous media, *IEEE Trans. Magn.* **MAG-21**, 2188 (1985).
38. J. Nédélec, Mixed finite elements in R^3, *Numer. Math.* **35**, 315 (1980).
39. J. Nédélec, A new family of mixed finite elements in R^3, *Numer. Math.* **50**, 57 (1986).
40. D. Sommerville, Space-filling tetrahedra in Euclidean space, *Prc. Edinburgh Math. Soc.* **41**, 49 (1923).
41. A. Taflove, *Computational Electrodynamics* (Artech House, Boston, 1995).
42. A. Taflove and K. R. Umashankar, Radar cross section of general three-dimensional scatterers, *IEEE Trans. Electromagn. Compat.* **EMC-25**, 433 (1983).
43. A. Wathen, Realistic eigenvalue nounds for the Galerkin mass matrix, *IMA J. Numer. Anal.* **7**, 449 (1987).
44. J. P. Webb and V. N. Kanellopoulos, Absorbing boundary conditions for the finite element solution of the vector wave equation, *IEEE Microwave Opt. Technol. Lett.* **2**, 370 (1989).
45. N. P. Wetherill and O. Hassan, Efficient grid generation using the Delaunay triangulation, in *Computational Fluid Dynamics '92,* edited by Ch. Hirsch *et al.* (Elsevier, Amsterdam, 1992).

46. J. A. Wheeler, Permafrost thermal design for the trans-Alaska pipeline, in *Moving Boundary Problems*, edited by D. G. Wilson, A. D. Solomon, and P. T. Boggs (Academic Press, New York, 1978), pp. 267–284.
47. J. Wood, *An Analysis of Mixed Finite Element Methods for Maxwell's Equations on Nonuniform Meshes*, Ph.D. thesis (Oxford University, Oxford, UK, 1994).
48. K. Yee, Numerical solution of initial boundary value problems involving Maxwell's equations in isotropic media, *IEEE Trans. Ant. Propagat.* **AP-16**, 302 (1966).
49. X. Yuan, D. Lynch, and K. Paulsen, Importance of normal field continuity in inhomogeneous scattering computations, *IEEE Trans. Microwave Theory Technol.* **39**, 638 (1991).